Astronomy
&
Astrophysics

An updated survey of globular clusters in M 31

I. Classification and radial velocity for 76 candidate clusters[⋆,⋆⋆]

S. Galleti[1,2], L. Federici[2], M. Bellazzini[2], A. Buzzoni[2], and F. Fusi Pecci[2]

[1] Università di Bologna, Dipartimento di Astronomia via Ranzani 1, 40127 Bologna, Italy
   e-mail: silvia.galleti2@unibo.it
[2] INAF – Osservatorio Astronomico di Bologna, via Ranzani 1, 40127 Bologna, Italy
   e-mail: [michele.bellazzini; luciana.federici; alberto.buzzoni; flavio.fusipecci]@oabo.inaf.it

ABSTRACT

Aims. We present the first results of a large spectroscopic survey of globular clusters and candidate globular clusters in the nearby M 31 galaxy. The survey is aimed at the classification of known candidate M 31 clusters and at the study of their kinematic properties.
Methods. We obtained low-resolution spectroscopy ($\lambda/\Delta\lambda \simeq 800 - 1300$) for 133 targets, including 76 yet-to-be-confirmed candidate clusters (i.e. with no previous spectroscopic information), 55 already-confirmed genuine M 31 clusters, and 2 uncertain candidates. Our observations allowed a reliable estimate of the target radial velocity, within a typical accuracy of $\sim\pm20$ km s^{-1}. The observed candidates have been robustly classified according to their radial velocity and shape parameters that allowed us to confidently discriminate between point sources and extended objects even from low-spatial-resolution imagery.
Results. In our set of 76 candidate clusters we found: 42 newly-confirmed bona-fide M 31 clusters, 12 background galaxies, 17 foreground Galactic stars, 2 Hɪɪ regions belonging to M 31 and 3 unclassified (possibly M 31 clusters or foreground stars) objects. The classification of a few other candidates not included in our survey has been also reassessed on various observational bases. All the sources of radial velocity estimates for M 31 known globular clusters available in the literature have been compared and checked, and a homogeneous general list has been obtained for 349 confirmed clusters with radial velocity.
Conclusions. Our results suggest that a significant number of genuine clusters ($\gtrsim100$) is still hidden among the plethora of known candidates proposed by various authors. Hence our knowledge of the globular cluster system of the M 31 galaxy is still far from complete even in terms of simple membership.

Key words. galaxies: individual: M 31 – galaxies: star clusters – galaxies: Local Group

1. Introduction

Since the beginning of extragalactic astronomy (Hubble 1932), the study of the globular cluster (GC) system around the Andromeda galaxy (M 31) stands out as an important field of investigation, providing the ideal counterpart to compare with the GC system of our own Galaxy and a testbed for observational techniques to be applied to GC systems of more distant galaxies. It is now possible to directly compare integrated properties and resolved Color Magnitude Diagrams (CMD) of M 31 clusters, as recently obtained with the Hubble Space Telescope (HST) (see, e.g. Fusi Pecci et al. 1996; Brown et al. 2004; Rich et al. 2005).
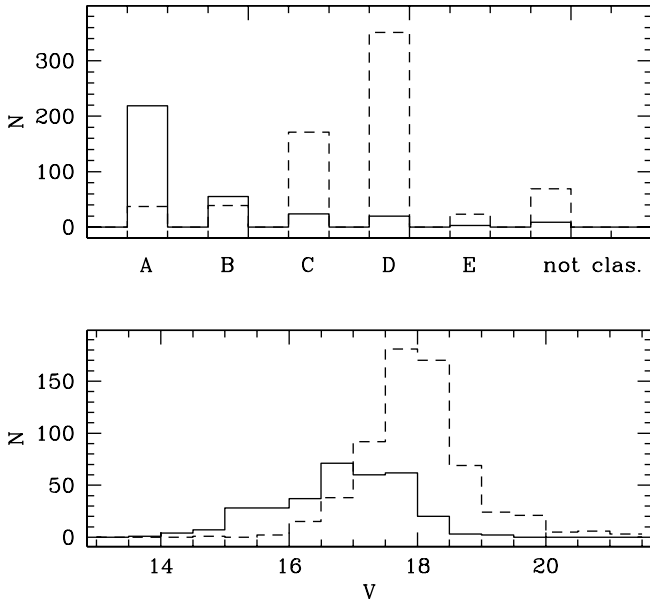
In spite of a similar mass and morphology, M 31 is recognized to display several differences in its stellar and clusters content with respect to the MW. For instance, the halo stellar populations of the two galaxies (the typical environment of most GCs) widely differ in average metallicity; while stars in the MW halo are predominantly metal poor ($\langle$[Fe/H]$\rangle \simeq -1.6$ dex (Laird et al. 1988), those in the outer regions of M 31 have $\langle$[Fe/H]$\rangle \simeq -0.5$ dex (see, for example, Holland et al. 1996; Bellazzini et al. 2003; Rich et al. 2004; Durrell et al. 2004, and references therein). The GC system of M 31 is much more populous than that of the MW, with more than 300 confirmed clusters, to compare with the ~150 of the MW. In particular, Barmby et al. (2001) estimated the total number of M 31 GCs to be 475 ± 25, i.e. more than a factor of three larger than in the Milky Way. It is clear that understanding the reasons for such striking differences may shed light on the formation histories of the two galaxies and on the general process of galaxy formation.

Since early systematic surveys (see, among others, Veteŝnik 1962; van den Bergh 1967, 1969; Baade & Arp 1964; Sargent et al. 1977; Crampton et al. 1985; Battistini et al. 1980, 1982, 1987, 1993; Sharov et al. 1995; Mochejska et al. 1998; Barmby et al. 2000, and references therein), most of the known M 31 GC candidates (hereafter GCCs) have been typically identified by visual inspection of wide-field photographic plates, and a more exhaustive analysis with CCD cameras is still partially lacking. A few recent studies (see, for example,

---

Fig. 1. Distribution of the original quality-class classifications of Battistini et al. (*upper panel*), and the *V* luminosity function (*lower panel*) for confirmed M 31 clusters (that is all $c = 1$ entries in the RBC – see Sect. 1 – according to G04; solid histogram) and candidate M 31 clusters ($c = 2$ RBC flag; dashed histogram). Note the huge number of yet-to-be-confirmed candidates at $V > 17.0$, mainly belonging to class C and D of the Battistini et al. classification scale.

Racine 1991; Barmby & Huchra 2001; Mochejska et al. 1998; Huxor et al. 2004, 2005; Barmby et al. 2001; Perrett et al. 2002; Fusi Pecci et al. 2005; Beasley et al. 2004; Puzia et al. 2005) have clearly shown that this kind of new-generation survey may significantly change our knowledge of the number and nature of the clusters harbored in the M 31 system. To date, there are still hundreds of known GCCs (~700, see Galleti et al. 2004, henceforth G04) whose nature remains to be ascertained.

Most of these candidates lie or pertain to the faint-end tail of the GC luminosity function which, at present, is far from complete (see Fig. 1). Battistini et al. (1980, 1982, 1987, 1993) ranked the majority of cluster candidates according to a quality class (from "A" to "E" in the sense of decreasing confidence level) related to their appearance on the original images. The upper panel of Fig. 1 shows that the majority of class A and B candidates have already been confirmed (either spectroscopically or, in a few cases, by high resolution images), while most of class C and D targets remain to be explored. One has to consider that any comprehensive sample of M 31 GCs relies on coarse databases whose homogeneity is difficult to assess. On the other hand, a catalog of M 31 clusters as complete and homogeneous as possible is clearly overdue, and this is a fundamental step for any meaningful comparison with other systems.

In G04 we re-analyzed the photometric and classification data available in the literature, reporting coarse photometry on a self-consistent CCD-based magnitude scale, and providing infrared information for several hundred GCCs, with *J*, *H*, *K* magnitudes from the 2MASS database (Skrutskie et al. 2006). The resulting catalog (Revised Bologna Catalog, hereafter RBC[1]) contains at present 1164 entries, including all the already

---

[1] The catalog is available electronically at
`http://www.bo.astro.it/M31/`.

confirmed clusters, the known but yet-to-be-confirmed candidates, and the proposed candidates whose "non-M 31-GC" nature has been definitely established. We believe that keeping record of the latter objects is very useful not only to avoid duplicating observations, but also to characterize the properties of the typical contaminants, to optimize selection criteria and maximize the return of future observational campaigns (see G04 for details and discussion).

We recall the RBC classification scheme, as originally used in G04. The classification flag c can assume the following values: $c = 1$ confirmed clusters, $c = 2$ candidate clusters, $c = 3$ uncertain candidates, $c = 4$ background galaxies, $c = 5$ HII regions, $c = 6$ foreground stars. In addition, as a result of the present discussion (see Sect. 4.3, below), we will also introduce a new class ($c = 7$) including asterisms/associations.

We are carrying out survey of GCCs located at large (projected) distance from the center of M 31, a nearly unexplored area. A first pilot run of the survey led to the discovery of B514 (Galleti et al. 2005, hereafter G05), the outermost cluster of the Andromeda galaxy yet known.

Finally we have undertaken a large spectroscopic follow-up of known candidates, to assess their nature and study their physical properties. This is the subject of the present paper, where we deal with classification and kinematic of 76 M 31 GCCs never surveyed before.

In Sect. 2 we briefly introduce the problem of M 31 GCC classification, and describe the observational material and its reduction procedures. Section 3 is devoted to radial-velocity estimates for our sample and the comparison of our results with other spectroscopic datasets available in the literature. Section 4 deals with the classification of the observed candidates and in Sect. 5 we use the kinematical information for the updated sample of confirmed clusters to estimate the mass of M 31. Finally, in Sect. 6 we summarize and discuss our results.

In a companion paper (Galleti et al., in preparation) we will complete our study by assessing the problem of a self-consistent metallicity scale for M 31 GCs, relying on homogeneous measures of the Lick indices (Trager et al. 1998).

2. Observations and data reduction

A spectroscopic database of 133 targets has been collected through different observing runs in 2004/05, carried out at the Roque de los Muchachos (La Palma, Spain) observing facilities of the 3.5 m Telescopio Nazionale Galileo (TNG) and the 4.2 m William Herschel telescope (WHT), and at the "G.B. Cassini" 1.52 m telescope of the Loiano Observatory (Italy). Our sample comprises 76 M 31 GCCs, while further 55 confirmed clusters ($c = 1$ RBC flag) were included to consistently match our results with other external data sources in the literature, together with 2 questioned objects that need a more definitive spectroscopic assessment. The survey aims at achieving accurate radial-velocity measurements for a wide sample of M 31 GCCs through low-resolution long-slit and fiber spectroscopy.

Kinematical information alone can easily discriminate between genuine M 31 GCs and the most relevant class of spurious contaminants, i.e. background galaxies. The nature of the latter sources can be recognized because of their cosmological recession velocities (typically $6000 \lesssim cz \lesssim 50\,000$ km s^{-1}, see G04), much larger (and opposite in sign) than the systemic velocity of M 31 (namely $V_r \simeq -301$ km s^{-1}, Van den Bergh 2000).

On the other hand, radial velocity alone may not be sufficient to discriminate between M 31 GCs and foreground interlopers – mostly MW stars – the other major source of contamination

in our sample. In these cases one has to recur to morphological criteria to confidently discriminate between point (i.e. stars) and extended sources (GCs). To assess this important point, we also complemented our spectroscopic analysis with supplementary imagery, taken at the Loiano telescope, for an independent but largely overlapping sample of 86 RBC objects. We will return in Sect. 4 to full discussion of these results.

2.1. WYFFOS data

Most of our sample has been observed during the nights of Nov. 21 and 22 2004, using the AutoFib2+Wide Field Fibre Optic Spectrograph (WYFFOS; Telting & Corradi 2000), mounted at the WHT prime focus. We adopted the R1200B grating, covering the $\lambda\lambda = 4000 \rightarrow 5700$ Å spectral range with a *FWHM* wavelength resolution of 2.2 Å. WYFFOS is equipped with a mosaic of two EEV-42-80 CCDs, windowed and mosaiced so as to have $\simeq 4300 \times 4200$ px^2 in total, that were read in 2×2 binning mode, with a scale of 0.4 Å/pixel. We used the Small Fibre module, which is made of 150 1.6 arcsec science fibres, and 10 fiducial bundles for target acquisition and guiding. Four different fibre configurations were set up in order to target a total of 183 confirmed clusters and GCCs.

A total of 10 science exposures ranging from 1200 to 2700 s were acquired (four in the first night and six in the second night). Calibrating exposures included bias, sky and lamp flat-field, and He/Ne comparison lamps. For each of the four pointings we typically allocated a fraction of ~30% of the whole fibre configuration to simultaneously sample the sky level. The sky emission was also probed before and after each target exposure by dithering the same fibre configuration. Data were processed in IRAF, using a dedicated package (WyffosREDUC) written by Pierre Leisy. The code was modified to automatically account for the whole data-reduction pipe-line; the procedure has been extensively tested, comparing the results with those obtained with standard reduction techniques for long-slit spectra. The WyffosREDUC package is based on the IRAF task DOFIBER, and corrects frames for bias, flat-field and for fiber throughputs, extracts spectra for each fibre, calibrates them in wavelength, and performs sky subtraction as described below. Fibre throughputs have been obtained from exposures of sky flat-field frames.

Sky correction needs special attention when dealing with fiber observations; in this regard we explored two independent techniques: *i)* a master sky spectrum was mapped by a grid of ~35 fibers homogeneously distributed across the whole field of view. This output was then subtracted from each science spectrum after rescaling for the appropriate fiber throughput; *ii)* the on-target shots were flanked (before and after) by two off-target images (dithering the telescope 20″ E away) to sample sky level with the same fiber configuration. No substantial differences were found between the two procedures (see Fig. 2 for an example), and we decided to apply option *(i)* for our analysis.

Two M 31 globular clusters (namely B225 and B158), for which very accurate radial velocity estimates are available in the literature (Dubath & Grillmair 1997), were observed in two different pointings and used as reference templates to set the radial-velocity zero point. These reference spectra reach $S/N > 50$ per pixel, to be compared with a typical $S/N \simeq 10$ for the GCC spectra. Two exposures for each scientific target were acquired. The same strategy has been adopted for the runs described below.

The poor seeing conditions (*FWHM* ~ 1.5″), in addition to thin-cloud sky coverage during both observing nights, and
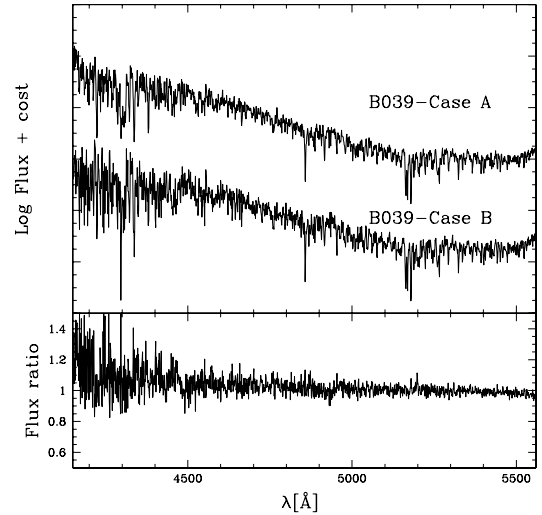
Fig. 2. An example of the impact of different sky-subtraction procedures on WYFFOS spectroscopic observations of cluster B039 *(upper panel)*. The raw instrumental spectrum is displayed after sky subtraction *i)* according to a "master spectrum" (Case A) homogeneously sampled across the whole field of view by ~35 suitably allocated fibres, and *ii)* by evaluating sky level from 20″ off-target dithered images taken with the scientific fiber configuration just before and after the on-target shot (Case B). An arbitrary offset in log *Flux* has been added to the data for graphical optimization. *Lower panel* – the flux ratio of Case A and B raw spectra. Global standard deviation (per pixel element) amount to a 9% (with no evident drift with wavelength), improving to a 4% scatter if we restrain λ to ≥ 4500 Å.

the less-than-perfect positioning of some fibres limited the final signal-to-noise of several faint targets. For this reason only 116 out of the 183 targets had a useful spectrum for our analysis.

2.2. BFOSC data

Long-slit spectra for 8 relatively bright ($V \leq 16.5$) targets were obtained with the low-resolution spectrograph BFOSC (Gualandi & Merighi 2001) operated at the Loiano Observatory. The detector was a thinned, back illuminated EEV CCD, with 1300×1340 px^2. The observations were carried out under typical seeing conditions (*FWHM* ~ 1.5″), on six nights during 2004 (Sep. 18–19, Nov. 16–17) and 2005 (Jan. 02–05). With a 1.5 arcsec slit, the adopted setup provided a *FWHM* spectral resolution $\Delta\lambda = 4.1$ Å ($\lambda/\Delta\lambda \simeq 1300$) covering the range $\lambda\lambda = 4200 \rightarrow 6600$ Å. We took a He-Ar calibration-lamp spectrum after each scientific exposure, maintaining the same telescope pointing. Exposure times were typically 45 min, yielding spectra with a characteristic $S/N \simeq 8$ per resolution element.

During each observing night and with the same instrumental setup, we also collected accurate ($S/N > 70$) observations of four radial-velocity template targets, namely the same M 31 GCs adopted for the WYFFOS run (B158 and B225) plus stars HD 12029 and HD 23169 (heliocentric radial velocities from the SIMBAD database). Bias, flat field, and sky subtraction were carried out using standard packages in IRAF, as described in Galleti et al. (2005).

2.3. DOLORES data

The imager/spectrograph DoLoRes at the TNG was used in the nights of Sep. 8 and Oct. 8, 2004, to acquire long-slit spectra of

9 M 31 GCCs. DoLoRes is equipped with a 2048×2048 px^2 thinned and back-illuminated Loral CCD array providing a $9.4' \times 9.4'$ field of view. The adopted MRB grism yielded a resolution of 6 Å *FWHM* ($\lambda/\Delta\lambda = 875$) with a 1″ slit, across a $\lambda\lambda = 3800 \rightarrow 6800$ Å spectral range. We typically exposed for 10–15 min, reaching $S/N \simeq 13$ per resolution element. A He-lamp spectrum was acquired after each science frame for wavelength calibration. During each night we obtained good ($S/N \gg 50$) spectra for the template clusters B158 and B225. The data reduction procedure was the same as for the BFOSC data.

3. Radial velocities

The heliocentric radial velocities (V_r) of GCCs were obtained by cross-correlation with the template spectra, using the IRAF/fxcor package (see Tonry & Davis 1979, for details of the technique). We applied a square filter to dampen the highest and lowest frequency Fourier components, that heavily masked the narrow peaks in the power spectrum. We then fitted the power peaks with Gaussians. The typical internal velocity errors on a single measure were ∼30 km s^{-1} for WYFFOS, ∼50 km s^{-1} for BFOSC and ∼ 65 km s^{-1} for DoLoRes spectra[2].

For each target we cross-correlated two independent spectra with (at least) four template spectra, obtaining ≥ 8 semi-independent estimates of radial velocity. We take the average of these values as our final V_r, and the standard deviation as our final uncertainty on V_r. The typical uncertainties are ∼14 km s^{-1} for WYFFOS data, ∼19 km s^{-1} for BFOSC, and ∼33 km s^{-1} for DoLoRes data.
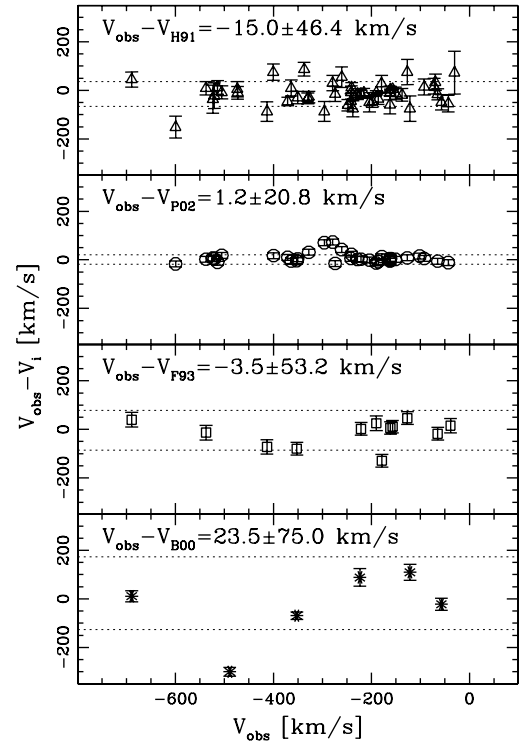
At the end of the analysis we obtained reliable V_r estimates for 133 targets (116 targets from WYFFOS data, 9 from DoLoRes data, and 8 from BFOSC data), 76 of which were previously unconfirmed GCCs. Of the latter, 12 objects were eventually classified as background galaxies due to their evident cosmological redshift and, in 9 cases, also to striking line emission in their spectra (see Sect. 4.2 for further details). Two more objects, G137 and G270, display clear Hβ, Hγ and [OIII] emission lines and a value of V_r compatible with M 31 HII regions (see, for a comparison, Diaz et al. 1987).

The list of the observed targets is reported in Table 1, together with their apparent V magnitude and $V - K$ color (Cols. 2 and 3, from G04), the estimated V_r and the associated uncertainty (Cols. 4 and 5), the original quality class (Col. 6), according to Battistini et al. (1982, 1987), and the instrument used to obtain the spectra (Col. 7).

3.1. Comparisons with previous studies

Our subsample of 57 already confirmed M 31 GCs in Table 1 allows a thorough comparison with other samples of radial velocities for M 31 clusters available in the literature (van den Bergh 1969, henceforth V69; Huchra et al. 1982; Huchra et al. henceforth H91 1991; Peterson 1989; Dubath & Grillmair 1997;

Fig. 3. Comparison of radial velocities from the present study (V_{obs}) with estimates from other authors (H91 = Huchra et al. 1991; P02 = Perrett et al. 2002; F93 = Federici et al. 1993; B00 = Barmby et al. 2000). In each panel we report the mean radial velocity difference and standard deviations between the two sets under consideration. 2-σ contours around the mean are also reported (dotted lines).

Federici et al. 1993, F93; Jablonka et al. 1998, J98; Barmby et al. 2000, B00; Perrett et al. 2002, P02).

This exercise has the twofold purpose of *i)* checking the reliability of our measures and their overall consistency with previous estimates; and *ii)* probing the mutual self consistency of different existing V_r datasets and trying to match each of them into a common radial-velocity scale. For this we need to recover the possible systematic offsets in the V_r zero points and provide a suitable average for those objects with redundant/multiple measurements, assessing the intrinsic accuracy of the different data sources.

To do that, it is useful to divide the overall database in two categories, i.e. V_r measurements coming from low-resolution spectroscopy ($\sigma(V_r) = 10$–100 km s^{-1}), and those derived from high-resolution echelle spectra ($\sigma(V_r) \ll 10$ km s^{-1}). Latter class includes the works of Dubath & Grillmair (1997) and Peterson (1989), who provided radial velocities of M 31 clusters with a notably high accuracy ($\sigma(V_r) \lesssim 3$ km s^{-1}) and excellent agreement for the objects in common. We therefore decided to merge both samples into a single High Resolution (HR) set of 24 clusters, referring however to the Dubath & Grillmair (1997) V_r value for the clusters in common. The HR set will provide the backbone of a comprehensive velocity scale joining measures from all the available sources.

In Fig. 3 we present a comparisons of our output for the cluster subsamples in common with the low-resolution observations by H91, P02, F93 and B00. In all cases the overall agreement is good, within the combined uncertainties of the two considered datasets. The comparison with H91 suggests the presence of a

---

[2] The standard cross correlation procedure provided poor results for background galaxies, given the reduced wavelength range in common with the reference template globulars and, in most cases, the presence of strong emission lines. For those targets with $V_r > +6000$ km s^{-1} we therefore derived the value of cz directly from the measure of a few strong emission/absorption spectral features like the [OII]3727, [OIII]5007, Ca HK, Hβ, Hδ, Hγ, and MgH lines. This led to higher (but still fully acceptable) uncertainties on the inferred value of cz in Table 1.

Table 1. Radial velocities of observed GCCs and GCs.

Name	V	$V-K$	$V_r \pm \sigma(V_r)$ [km s^{-1}]		qc[†]	Instrum.	Name	V	$V-K$	$V_r \pm \sigma(V_r)$ [km s^{-1}]		qc[†]	Instrum.
							NB70	14.89	2.47	−17 ±	11	E	BFOSC
Previously unconfirmed Globular Cluster Candidates							SH01(*)	15.82		21 500 ±	600		BFOSC
B003	17.57	2.03	−351 ±	11	A	WYFFOS	B295D	17.86	3.69	32 600 ±	600	D	WYFFOS
B022	17.36	1.85	−407 ±	14	A	WYFFOS	B330D	15.99	1.59	−62 ±	18	D	BFOSC
B032	17.61	3.55	−516 ±	8	B	WYFFOS	BA21(*)	16.64	2.77	36 600 ±	1400		BFOSC
B060	16.75	2.61	−484 ±	25	A	WYFFOS	G137(*)	17.81		−256 ±	28		WYFFOS
B067	17.25	1.99	−377 ±	10	A	DoLoRes	G270(*)	17.30		−72 ±	23		WYFFOS
B070	17.07	2.25	−301 ±	15	A	WYFFOS	H126	16.76	1.77	−19 ±	20		WYFFOS
B071	17.79		−479 ±	8	B	WYFFOS	M049	18.26	2.66	−247 ±	17	D	WYFFOS
B077	17.50	2.94	−681 ±	25	A	DoLoRes	Previously observed controversial objects						
B087	17.93		−382 ±	16	B	WYFFOS	B341	16.37	2.84	−352 ±	32	A	BFOSC
B099	16.74	3.15	−200 ±	11	A	WYFFOS	B409	12.53	2.00	−39 ±	10	A	BFOSC
B100	17.91	3.22	−376 ±	25	B	WYFFOS	Previously confirmed Globular Clusters						
B111	16.80	2.27	−414 ±	10	A	WYFFOS	B006	15.50	2.87	−228 ±	14	A	WYFFOS
B155	17.97	3.25	−401 ±	34	B	WYFFOS	B012	15.09	2.35	−364 ±	3	A	WYFFOS
B162	17.48	3.65	−146 ±	8	A	WYFFOS	B017	15.95	3.36	−505 ±	10	A	WYFFOS
B168	17.63	4.11	−190 ±	14	B	WYFFOS	B019	14.93	2.95	−221 ±	7	A	WYFFOS
B169	17.08	3.14	−177 ±	7	A	WYFFOS	B034	15.47	2.97	−537 ±	8	A	WYFFOS
B187	17.17	2.85	−130 ±	10	A	WYFFOS	B039	15.98	3.60	−242 ±	16	A	WYFFOS
B189	16.99	3.34	−148 ±	8	A	WYFFOS	B042	16.29	4.13	−279 ±	26	A	WYFFOS
B194	17.19	2.08	−354 ±	21	A	WYFFOS	B051	16.08	3.25	−274 ±	8	A	WYFFOS
B215	17.13	2.90	−164 ±	3	A	WYFFOS	B073	15.99	2.89	−473 ±	44	A	WYFFOS
B245	16.56	2.99	6200 ±	1400	C	WYFFOS	B082	15.54	4.09	−371 ±	7	A	WYFFOS
B247	17.66		−532 ±	17	C	WYFFOS	B083	17.09	2.48	−296 ±	19	A	WYFFOS
B248	17.84	1.94	−524 ±	21	C	WYFFOS	B095	15.81	3.35	−238 ±	11	A	WYFFOS
B253	18.01	1.76	−722 ±	35	C	DoLoRes	B110	15.28	3.01	−241 ±	7	A	WYFFOS
B265	17.58	2.10	−496 ±	16	C	WYFFOS	B117	16.34	2.46	−524 ±	25	A	WYFFOS
B348	16.79	2.84	−170 ±	5	B	WYFFOS	B131	15.44	2.82	−337 ±	0	A	WYFFOS
B362	17.61	2.09	−81 ±	4	A	WYFFOS	B148	16.05	2.88	−261 ±	16	A	WYFFOS
B371	17.54		−127 ±	18	B	WYFFOS	B151	14.83	3.47	−330 ±	2	A	WYFFOS
B388	17.96	3.17	−50 ±	9	B	WYFFOS	B153	16.24	3.15	−248 ±	19	B	WYFFOS
B419(*)	18.19	2.69	41 600 ±	600	C	DoLoRes	B156	16.90		−400 ±	0	A	WYFFOS
B425(*)	17.52	2.74	16 900 ±	600	C	DoLoRes	B158	14.70	2.89	−190 ±	13	B	WYFFOS
B469(*)	17.58	2.60	21 900 ±	600	C	WYFFOS	B163	15.04	3.36	−157 ±	23	A	WYFFOS
B471	17.12	3.63	30 200 ±	1200	C	WYFFOS	B174	15.47	2.98	−473 ±	16	A	WYFFOS
B473	17.46	1.51	11 ±	14	C	WYFFOS	B176	16.52	2.41	−521 ±	5	A	WYFFOS
B020D	17.44	3.43	−526 ±	21	D	WYFFOS	B178	15.03	2.41	−138 ±	6	A	WYFFOS
B021D	17.50	2.59	6 ±	7	D	WYFFOS	B179	15.39	2.58	−151 ±	8	A	WYFFOS
B022D	17.80		−354 ±	24	D	WYFFOS	B180	16.02	2.62	−204 ±	13	A	WYFFOS
B025D	17.83	3.88	−479 ±	25	D	WYFFOS	B182	15.43	2.98	−328 ±	12	A	WYFFOS
B027D	17.60	1.61	−50 ±	7	D	WYFFOS	B183	15.95	2.95	−179 ±	14	A	WYFFOS
B034D	17.50	2.97	−347 ±	25	D	DoLoRes	B185	15.54	2.90	−162 ±	7	A	WYFFOS
B036D	17.10		−54 ±	7	D	WYFFOS	B193	15.33	3.18	−65 ±	5	A	WYFFOS
B041D	17.90	2.65	−289 ±	11	D	WYFFOS	B201	15.90	2.47	−689 ±	17	A	WYFFOS
B045D	18.30	2.66	−313 ±	16	D	WYFFOS	B204	15.75	2.94	−351 ±	11	A	WYFFOS
B046D	17.00		−327 ±	24	D	WYFFOS	B206	15.06	2.57	−198 ±	13	A	WYFFOS
B071D	17.60	2.04	−229 ±	11	D	WYFFOS	B212	15.48	2.35	−413 ±	10	A	WYFFOS
B073D	17.90		−12 ±	13	D	WYFFOS	B219	16.39	2.92	−514 ±	15	A	WYFFOS
B079D	17.80		−394 ±	25	D	WYFFOS	B224	15.45	2.06	−162 ±	17	A	WYFFOS
B090D	17.20	3.63	−94 ±	8	D	WYFFOS	B225	14.15	3.08	−161 ±	13	A	WYFFOS
B096D	17.30	3.96	−203 ±	15	D	WYFFOS	B228	16.78	3.01	−400 ±	41	A	WYFFOS
B109D	17.00		−8 ±	15	D	WYFFOS	B229	16.47	2.22	−31 ±	5	A	WYFFOS
B126D	18.00	2.98	−92 ±	8	D	WYFFOS	B230	16.05	2.23	−600 ±	5	A	WYFFOS
B147D(*)	17.96		38 800 ±	600	D	DoLoRes	B232	15.67	2.40	−186 ±	9	A	WYFFOS
B148D(*)	16.31	2.20	16 800 ±	300	D	BFOSC	B233	15.76	2.59	−72 ±	9	A	WYFFOS
B158D(*)	16.50	2.69	16 800 ±	300	D	DoLoRes	B235	16.27	2.96	−92 ±	15	A	WYFFOS
B168D(*)	18.45		38 600 ±	600	D	DoLoRes	B236	17.38		−411 ±	31	A	WYFFOS
B213D	17.07	1.73	19 ±	9	D	WYFFOS	B238	16.42	2.73	−43 ±	14	A	WYFFOS
B215D	16.79	2.53	−266 ±	12	D	WYFFOS	B240	15.21	2.42	−57 ±	6	A	WYFFOS
B217D	17.88	2.14	−136 ±	9	D	WYFFOS	B344	15.95	2.58	−240 ±	16	A	WYFFOS
B221D	17.77	3.32	−50 ±	8	D	WYFFOS	B347	16.50	2.37	−224 ±	24	A	WYFFOS
B226D	17.89	3.38	−9 ±	8	D	WYFFOS	B356	17.34	3.07	−179 ±	13	A	WYFFOS
B237D	18.02	2.82	10 ±	8	D	WYFFOS	B366	15.99	2.01	−127 ±	21	A	WYFFOS
B243D	18.05	2.14	−53 ±	18	D	WYFFOS	B373	15.64	3.15	−215 ±	13	A	WYFFOS
B250D	17.46	4.31	−442 ±	21	D	WYFFOS	B377	17.14	2.68	−121 ±	32	B	WYFFOS
B255D	17.92		−107 ±	14	D	WYFFOS	B381	15.76	2.69	−69 ±	14	A	WYFFOS
B260D	17.07	2.45	−93 ±	6	D	WYFFOS	B472	15.19	2.56	−101 ±	8	C	WYFFOS
B275D	18.11	2.26	−13 ±	6	D	WYFFOS	B514	16.28	2.62	−458 ±	23	A	BFOSC
NB65	16.26	2.55	8 ±	6	E	WYFFOS							

(*): Sources with line-emission spectrum; (†): original quality-class flag according to Battistini et al. (1980, 1982, 1987).

small systematic difference, also confirmed by the comparison with HR measures. The agreement with P02 is particularly good. Since the typical accuracy of this set is very similar to ours, the relatively low dispersion around the mean ($\sigma = 20.8$ km s^{-1}) is further support to our estimated V_r uncertainty. The large scatter of the differences to V_r estimates by B00 is not particularly satisfactory, but the small number of clusters in common prevents any further conclusion. Unfortunately, none of the HR cluster is included in the B00 sample. The comparison of the B00 velocities with the P02 sample (not shown here) reveals a good general
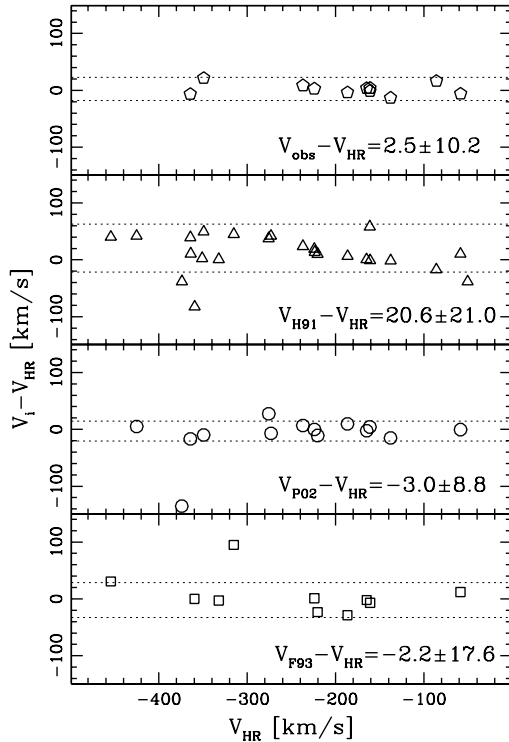
Fig. 4. Comparisons of radial velocities from low-resolutions studies with high-resolution estimates by Peterson (1989) and Dubath & Grillmair (1997). The mean differences and standard deviations after 2-σ clipping are indicated in each panel. 2-σ contours around the mean are also reported (dotted lines).

agreement but also several cases of serious inconsistency with 7 out of 21 clusters in common exceeding a ±100 km s^{-1} difference in the velocity estimates.

3.2. Consistency checks: towards a single homogeneous list of radial velocities

The comparisons with the HR set are presented in Fig. 4, where each panel reports the mean V_r difference and standard deviation for the different samples after a 2-σ clipping iteration.

The agreement of our V_r estimate with the HR ones, for the 12 clusters in common, is excellent. There is no sizable zero-point difference and again the standard deviation demonstrates the good accuracy of our measures. The same is true for the P02 and the F93 sets, although the latter shows a larger scatter due to the lower intrinsic accuracy of the data. The match with the H91 sample confirms, on the contrary, the presence of a systematic offset, as already suggested before and noted by H91 themselves. We applied the zero-point correction of Fig. 4 to this dataset, while we left untouched the P02 and F93 samples, the zero-point differences being much smaller than the involved statistical uncertainties. For the B00 and J98 data, both samples have no clusters in common with the HR sample and we had to compare them with other low-resolution observations. No systematic offset is needed, although one should notice several cases of striking outliers in each sample.

V69 presented a list of radial velocities for 44 bright M 31 GCs and GCCs. The comparison with the HR velocities for the 19 clusters in common reveals a small systematic offset ($V_{V69} - V_{HR} = -15.3 \pm 28.0$ km s^{-1}), after one outlier rejection.

Since all of the V69 targets have been re-observed by several authors in more recent studies, typically with better accuracy, we retain the V69 estimates only as an external check for controversial cases.

Once verified the self-consistency of all the available datasets we merged all the sources into one catalog of M 31 cluster radial velocities, tied to the HR set. This resulted from a weighted average of multiple measures, carefully checked on a cluster-by-cluster basis. In general, a weighted mean was iterated after 2-σ clipping. When only two incompatible measures (at >2σ) were available, we chose the one with lowest uncertainty. The overall compatibility among multiple measurements from different sources is, in general, very good. We found 18 cases of marginal >2σ deviation of one measure and 9 cases of serious incompatibility, a few of which were noted by P02. The latter nine cases probably deserve further verification and for B104 we adopted $V_r = -395 \pm 10$ km s^{-1} from B00, while J98 reports $V_r = +120 \pm 42$ km s^{-1}; for B109 we adopted $V_r = -372 \pm 12$ km s^{-1} from P02 while H91 reports $V_r = -633.6 \pm 24$ km s^{-1}; for B064D[3] we adopted $V_r = -72 \pm 10$ km s^{-1} from B00 while J98 reports $V_r = +191.0 \pm 62$ km s^{-1}; for B119 we adopted the weighted mean between the estimates by P02 and J98, $V_r = -310.1 \pm 11.1$ km s^{-1}, rejecting $V_r = -137 \pm 10$ km s^{-1} by B00; for B124 we adopted $V_r = +70 \pm 13$ km s^{-1} from B00, while J98 reports $V_r = -75 \pm 22$ km s^{-1} (the possibility of a graphical error should also be considered in this case); for B301 we adopted the weighted mean between the estimates by P02 and F93 $V_r = -381.9 \pm 10.9$ km s^{-1}, rejecting $V_r = -30 \pm 20$ km s^{-1} by B00; for B337 we adopted $V_r = +50 \pm 12$ km s^{-1} from B00, while F93 reports $V_r = -232 \pm 26$ km s^{-1}; for B350 we adopted the weighted mean between the estimates by B00 and H91 $V_r = -467.3 \pm 12.7$ km s^{-1}, rejecting $V_r = -251.7 \pm 26$ km s^{-1} by F93; for B380 we adopted $V_r = -13 \pm 12$ km s^{-1} from P02 while B00 reports $V_r = -121 \pm 31$ km s^{-1}. At least for the cases in which only two incompatible estimates are available (B104, B109, B124, B337, B380, B064D), a third independent estimate is highly desirable. Also among the 18 cases of weaker incompatibility there are four cases in which we had to choose between two estimates based on the accuracy of single estimates alone (B008, B047, B144, B314). For B131 we obtained $V_r = -337 \pm 3.0$ km s^{-1} while H91 report $V_r = -444.6 \pm 28$ km s^{-1}; for this case we revisited V69 reporting $V_r = -450$ km s^{-1}, supporting the H91 estimate that we eventually adopted.

In the following we will use the merged dataset described above as our source of V_r measures for M 31 GCs.

4. Classification

Figure 5 displays the radial velocity distribution of confirmed M 31 GCs (empty histogram). The distribution is centered on the galaxy systemic velocity (i.e. $V_s = -301.0$ km s^{-1}, van den Bergh 2000) and has a standard deviation $\sigma \simeq 160.0$ km s^{-1}. The distribution is significantly flatter than a Gaussian curve because most of M 31 GCs partake in the overall disk rotation around the galaxy center (see B00 and references therein). As we mentioned in Sect. 2, on the basis of the kinematical information, distant background galaxies can easily be excluded as they typically have $V_r \gg +300$ km s^{-1}.

To study the contamination by foreground MW stars we obtained a synthetic sample of Galactic stars over the magnitude range $16.0 \le V \le 19.0$, as spanned by our 76 GCCs, in a field of $3° \times 3°$ around the position of M 31, from the Besançon Galactic

---

[3] See updates and revisions http://www.bo.astro.it/M31/..
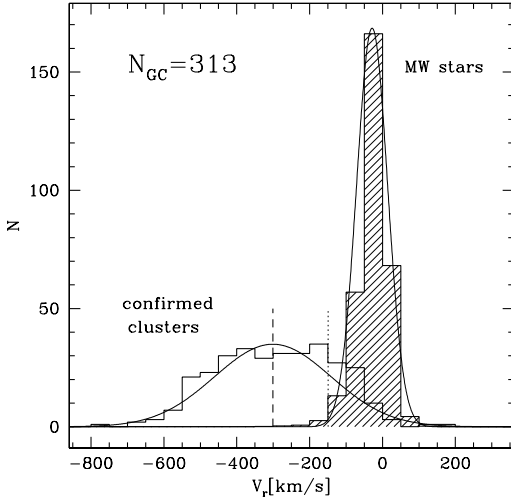
Fig. 5. Velocity distribution of confirmed M 31 clusters. The adopted systemic velocity of M 31 is marked by a dashed segment; the dotted segment marks the radial velocity threshold beyond which the contamination by foreground stars may become a serious issue. A Gauss curve with mean $\mu = -301.0$ km s^{-1} and standard deviation $\sigma = 160.0$ km s^{-1} is also superposed. The dashed histogram is the distribution of Galactic stars as predicted by the Besançon model (Robin et al. 2003), under the assumptions described in Sect. 4. A Gauss curve with mean $\mu = -29.0$ km s^{-1} and standard deviation $\sigma = 42.6$ km s^{-1} is also superposed.

Model (Robin et al. 2003). Down to this magnitude limit and across the observed field the synthetic sample predicts more than 10^4 stars; their radial velocity distribution is approximately Gaussian, with mean $\langle V_r \rangle = -29.6$ km s^{-1} and $\sigma = 42.6$ km s^{-1}, in excellent agreement with the sample of confirmed stars in the RBC (G04).

Since the available sample of confirmed GCs (obviously) has not been obtained from the observation of all the sources down to $V = 19.0$ in a $3° \times 3°$ field, a direct comparison between the two samples would be greatly misleading. As a reasonable and conservative normalization, we assume that the global catalog of 1164 objects contains as many foreground stars as (presently) confirmed GCs having V_r estimates, i.e. 313 stars. To limit the effects of fluctuations due to low-number statistics, we extracted at random from the whole synthetic catalog 100 samples of 313 stars and we obtained the V_r distribution for each of them. The shaded histogram is the average of these 100 distributions.

From Fig. 5 it can be safely concluded that GCCs with $V_r \leq -301.0$ km s^{-1} cannot be MW stars, hence they must be bona fide M 31 clusters. According to the above assumptions the expected number of MW stars with $-301.0 < V_r \leq -150.0$ km s^{-1} is ≤ 4, i.e. $\sim 1\%$ of the whole sample. On the other hand, for $V_r > -150.0$ the contamination by MW stars is likely very significant, preventing a fully reliable discrimination between foreground stars and M 31 GCs based on the radial velocity alone. According to these considerations, we decided to classify as bona fide M 31 GCs all the candidates with $V_r \leq -150.0$ km s^{-1}, requiring further investigation for those with higher V_r (see Sect. 4.1, below). Note that our approach is more conservative than the majority of previous studies that, in general, considered as genuine M 31 GCs all the candidates with velocity within $\sim \pm 3\sigma$ of the systemic velocity of M 31, in absence of clear evidence of discriminating features in the spectra and/or HST imaging revealing the stellar nature of the

candidate (see, for example, B00, P02). On the contrary, Fig. 5 strongly suggests that GCCs with V_r around $\sim -30.0 \pm 120$ km s^{-1} (65 objects in the RBC database, most of them "confirmed" GCs by virtue of their radial velocity alone) should be very carefully considered as they might likely include a certain fraction of misclassified MW stars. Clearly, any observation assessing the non-pointlike nature of these objects would be extremely valuable (see Sect. 4.1, below).

Using the above described criteria, for our 76 GCCs of Table 1 we are left with

(a) 35 genuine M 31 GCs with $V_r \leq -150.0$ km s^{-1};
(b) 12 background galaxies, with high recession velocity and/or line-emission spectra;
(c) 2 M 31 Hɪɪ regions (never observed before);
(d) 27 candidates, with $-150.0 < V_r < +100$ km s^{-1}, possibly compatible both with M 31 GCs *and* with MW stars, that will be further analyzed in the following[4].

4.1. Source morphology and foreground star contamination

To further investigate the nature of the 27 GCCs of item "d" above we acquired deep white-light BFOSC images of each field. In imaging mode, BFOSC has a pixel scale of 0.58″/px and a total field of view of $13.0' \times 12.6'$. All the observations were obtained in 2005, during the nights of Aug. 7–9, Sep. 2, 11 and 29, Oct. 4 and Nov. 7. The exposure times ranged between 3 and 10 min, depending on target brightness and atmospheric conditions. The nights were clear (but not photometric) with a typical seeing around 1.5–2 arcsec *FWHM*.

The pointings were accurately chosen in order to include in each frame one (or more) of the 27 targets and a number of confirmed M 31 GCs. This allowed us to extend our morphological analysis to a supplementary sample of 56 "confirmed" GCs plus 3 controversial targets[5].

Images have been bias and flat-field corrected with standard reduction procedures. Relative photometry, *FWHM* and morphological parameters of each source in the frame – down to a 5σ threshold over sky noise- were obtained with Sextractor (Bertin & Arnouts 1996). Only non-saturated and isolated sources were retained in the final catalogs (Sextractor quality flag "0").

In spite of the limited spatial resolution of the images, a fair assessment of the GCC morphology was made possible by a purely differential approach relying on the comparison with accurate point-spread function (PSF) estimates and on the study of the apparent isophotal radius of the detected objects. The relatively wide field of view of BFOSC allowed a simultaneous high-S/N imagery of the target together with hundreds of field stars, and at least a few confirmed M 31 GCs. Hence, the nature of the considered candidate was established by direct comparison with surrounding stars and extended sources *on the same frame*.

In particular, the apparent target size was probed *a)* in terms of its relative excess compared to the local PSF (namely, by defining a ratio parameter $R = $ [target *FWHM*]/[PSF *FWHM*])

---

[4] According to our constraints on the value of V_r, the controversial object B341 in Table 1 (class $c = 3$ in the original RBC classification) should be in the bona fide confirmed M 31 GCs supporting the original classification by P02. The case of B409 deserves further discussion (see Sect. 4.1.4).

[5] We also verified a posteriori that, out of these 59 objects, 13 further entries from Table 1 were serendipitously imaged. They are B042, B100, B193, B224, B228, B229, B232, B240, B265, B344, B347, B366, B045D (see Table 2).

Table 2. Morphological analysis for previously confirmed M 31 GCs.

Name	$V_r \pm \sigma(V_r)$ [km s^{-1}]		R	F-A flag	$c^{(\dagger)}$	Name	$V_r \pm \sigma(V_r)$ [km s^{-1}]		R	F-A flag	$c^{(\dagger)}$
B213	−545 ±	11	1.15	E	1	B347	−251 ±	20	1.14	E	1
B265	−496 ±	16	1.10	E	1	B048	−251 ±	12	1.22	E	1
B209	−460 ±	11	1.18	E	1	B220	−247 ±	12	1.75	E	1
B015D	−445 ±	12	1.31	E	1	B167	−231 ±	10	1.15	E	1
B093	−447 ±	12	1.25	E	1	B075	−212 ±	12	1.38	E	1
V031	−433 ±	12	2.33	E	1	B203	−199 ±	12	1.99	E	1
B161	−413 ±	12	1.20	E	1	B154	−199 ±	33	1.40	E	1
B221	−406 ±	12	1.24	E	1	B188	−184 ±	12	1.28	E	1
B021	−403 ±	12	1.29	E	1	B232	−182 ±	7	1.09	E	1
B228	−457 ±	26	1.43	E	1	B224	−161 ±	2	2.21	E	1
B100	−376 ±	25	1.45	E	1	B200	−153 ±	12	2.12	E	1
B467	−342 ±	12	1.26	E	1	B184	−152 ±	12	1.39	E	1
B043D	−344 ±	12	1.51	E	1	B367	−152 ±	12	1.07	E	1
B037	−338 ±	12	1.30	E	1						
B042	−338 ±	10	1.14	PS	1	B103D	−148 ±	12	1.18	E	1
B401	−333 ±	23	1.26	E	1	B240D	−148 ±	12	5.83	E	1
B059	−332 ±	12	1.24	E	1	B366	−141 ±	10	1.00	E	1(3)
B391	−325 ±	12	3.73	E	1	B272	−120 ±	12	1.53	E	1
B045D	−313 ±	16	1.22	E	1	B355	−114 ±	12	0.99	PS	1(6)
B024	−310 ±	34	1.09	E	1	B198	−105 ±	12	1.20	E	1
B222	−303 ±	10	1.36	E	1	B046	−98 ±	49	1.13	E	1
B382	−302 ±	12	1.12	E	1	B216	−93 ±	10	1.36	E	1(7)
B164	−294 ±	12	1.20	E	1	B072	−89 ±	12	2.52	E	1
B091	−290 ±	12	1.31	PS	1	B190	−86 ±	12	1.17	E	1
B047	−291 ±	12	1.19	E	1	B193	−59 ±	2	1.07	E	1
B354	−283 ±	26	1.14	E	1	B240	−56 ±	5	1.23	E	1
B210	−265 ±	12	1.18	E	1	B229	−31 ±	5	1.36	E	1
B214	−258 ±	12	1.12	E	1	B197	−9 ±	12	1.27	E	1
B344	−252 ±	13	1.34	E	1						

($\dagger$) New classification flag, according to the RBC notation (see also Sect. 1). The newly determined class of the three object for which we modify previous classification is reported in parentheses.

and *b*) in terms of its departure from the isophotal flux (F) vs. isophotal area (A) empirical relationship for stars to be suitably set in each individual frame according to the overall image quality[6]. Both F and A are natural outputs of Sextractor (respectively FLUX_ISO and ISOAREA_IMAGE parameters), and one could verify empirically that essentially all stars roughly obey a $A \propto F^{1/2}$ relationship being enclosed within a 0.1 dex wide strip in the $\log F$ vs. $\log A$ plane, corresponding to a variation of the measured *FWHM* of ±5% (see Fig. 6). Of course, hot pixels and cosmic rays appear as off-strip "sub-point-like" objects, while any source significantly more extended than the stellar PSF stands out in the F-A plot for its larger apparent size for a given magnitude level. To some extent, our approach recalls the classical diagnostic tools used, for instance, for high-redshift galaxy recognition (e.g. Kron 1980; Koo et al. 1986; Molinari et al. 1990).

Figure 6 is an example for a field matching two GCCs (open pentagons) and five already confirmed clusters (solid triangles). While all the five confirmed GCs are univocally identified as extended objects in the F-A plane, one of the candidates appears as an extended source, while the other one is compatible with a stellar point source. Accordingly, from the inspection of the individual F-A diagrams, we assigned to all the 27 candidates under consideration the flag E (extended) or PS (point source).

[6] Note that the limiting isophote is set at a $S/N = 5$ ratio per pixel element on each frame. This corresponds, in general, to a different surface brightness magnitude depending on image quality and sky conditions.

In the following we will refer to this flag as the F-A flag or, for brevity, the flag.

The R parameter and the F-A plane provide two complementary tools to judge the candidate extension since R is mainly sensitive to the core of the target image, while A, as the area within the outermost isophote, is more sensitive to the wings of the image. This is very well suited to study GC candidates since profiles of globular clusters may vary significantly, depending on their concentration parameter C (King 1966). For instance, high concentration clusters may have such compact cores that are indistinguishable from point sources but a significant difference with respect to genuine point sources can be detected looking at the wings of the image, sampling the faint halo of the cluster (see Buonanno et al. 1982).

It may be useful to have an idea of the sensitivity of the adopted technique, i.e. the size of the most compact M 31 GC that can be recognized as an extended object by our diagnostics. To this aim we performed a series of tests using the half-light radii (r_h) of globular clusters as the characteristic scale that is more appropriate in this context. According to Djorgovski (1993), half-light radii of Galactic GCs range from 0.8 pc to 20 pc, and more than 75% of his sample (118 GC with estimates of the half-light radius) have $r_h > 2.0$ pc. We translated these linear radii into angular radii at the distance of M 31 ($D = 783$ kpc, see Sect. 5.1, below) and we convolved them with the Half Width at Half Maximum (HWHM) of the PSF of our images. Finally, we found the minimum r_h that provides a
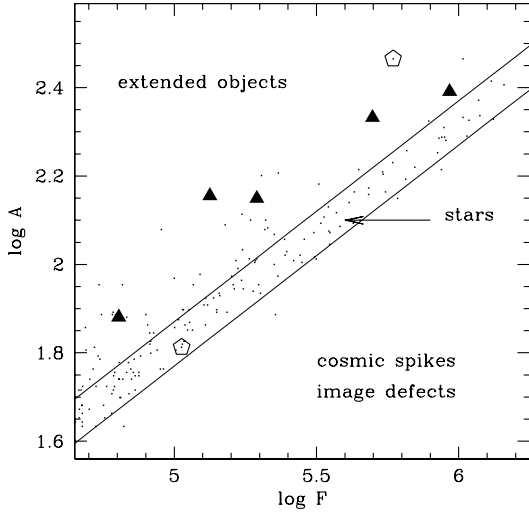
Fig. 6. F-A diagram for one of the images we analyzed (as an example). All the detected sources are plotted as small points. Filled triangles correspond to already confirmed clusters, empty pentagons to the candidate clusters under consideration. The continuous lines enclose the locus of points sources. Extended objects are expected to populate the upper left corner above the strip, while cosmic spikes and CCD cool/hot pixels must be confined to the lower right corner of the plot.

convolved profile larger than that of a point source by a factor ≥ 1.05. We are able to pick up clusters having r_h as small as 1.5 pc (corresponding to $0.4''$, at the distance of M 31), if the seeing is $2.0''$ *FWHM*, and we are sensitive to $r_h > 2.0$ pc if the seeing is $3.0''$ *FWHM*. Note that the radii of the isophotes adopted to compute ISOAREA_IMAGE are typically a factor of 2 larger than half-light radii, hence the effective sensitivity of the F-A diagram should be significantly better than these figures. This is confirmed by a direct comparison that can be made on three M 31 clusters included in the present programme that have an estimate of r_h from HST data (Barmby & Huchra 2001), namely B167 ($r_h = 0.33''$), B232 ($r_h = 0.66''$), and B240 ($r_h = 0.80''$). All of them are clearly identified as extended objects in the F-A diagram and their R parameters are 1.15, 1.09 and 1.23, respectively (see Table 2). Therefore, we conclude that the image analysis technique adopted here is able to recognize the extended nature of the large majority of M 31 clusters even with low-resolution images, provided that the target image is of high signal-to-noise ratio so that the image profile is well constrained.

4.1.1. Checking previously confirmed "genuine" clusters with $V_r \leq -150.0$

Table 2 reports the results of the image analysis described above for the M 31 clusters previously confirmed by other authors that were included in our BFOSC imaging survey. The first 42 entries in the table concern clusters that have $V_r \leq -150.0$ km s^{-1}, and can be unambiguously identified as genuine GCs on the basis of their radial velocity alone, according to our previous arguments. We note that all of them have $R \geq 1.07$, and all except three have $R \geq 1.10$. Only two clusters obtain the PS flag based on their position in the F-A diagram, but both of them have quite large R, 1.14 and 1.31 for B042 and B091, respectively. Hence our morphologic criteria correctly recognize all the genuine M 31 GCs considered here as extended objects.

Table 3. Morphological analysis for the 27 M 31 globular clusters candidates of Table 1 with $V_r > -150.0$ km s^{-1}.

Name	$V_r \pm \sigma(V_r)$ [km s^{-1}]		Class[a]	R[b]	F-A flag[c]	c[d]
B189	−148 ±	8	A	1.26	E	1
B162	−146 ±	8	A	1.27	E	1
B217D	−136 ±	9	D	0.94	PS	6
B187	−130 ±	10	A	1.47	E	1
B371	−127 ±	18	B	1.38	E	1
B255D	−107 ±	14	D	2.5	E	1
B126D	−92 ±	18	D	1.00	PS	6
B090D	−94 ±	8	D	1.15	E	1
B260D	−93 ±	6	D	1.03	PS	6
B362	−81 ±	4	A	1.09	PS	3
B330D	−62 ±	18	D	1.01	PS	6
B036D	−54 ±	7	D	0.99	PS	6
B243D	−53 ±	18	D	1.03	PS	6
B388	−50 ±	9	B	1.34	E	1
B027D	−50 ±	7	D	0.99	PS	6
B221D	−50 ±	8	D	1.05	PS	6
H126	−19 ±	10	/	1.06	PS	3
NB70	−17 ±	11	E	1.02	PS	6
B275D	−13 ±	6	D	0.98	PS	6
B073D	−12 ±	13	D	1.02	PS	6
B226D	−9 ±	8	D	1.00	PS	6
B109D	−10 ±	15	D	1.03	PS	6
B021D	6 ±	7	D	0.95	PS	6
NB65	8 ±	6	E	1.03	PS	6
B237D	10 ±	8	D	1.03	PS	6
B473	11 ±	7	E	1.00	PS	6
B213D	19 ±	9	D	1.06	PS	3

[a] Quality flag according to the Battistini et al. (1980; 1982; 1987; 1993) classification scale; [b] Target apparent size, relative to the PSF (namely $R = $ [target *FWHM*]/[PSF *FWHM*]; [c] E(xtended) or P(oint) S(ource) classification obtained from the F-A diagram; [d] RBC classification flag as in Table 2 (see Sect. 1).

Table 4. Candidates with controversial classifications.

Name	$V_r \pm \sigma(V_r)$ [km s^{-1}]	R	F-A flag	c
B055	−308 ± 8	1.27	E	1
B121	−24 ± 33	1.08	PS	3
B409	−40 ± 10	1.00	PS	6

Also based on these results, we can complete our classification scheme and devise the following supplementary criteria for GCCs with $V_r > -150.0$ km s^{-1}:

(a) a candidate is classified as a "bona fide M 31 cluster" ($c = 1$ in Tables 2–4) if $R \geq 1.10$, independently of the assigned flag, or if $R > 1.05$ and F-A flag "E";

(b) It is classified as a "bona fide star" ($c = 6$) if $R \leq 1.05$ and F-A flag "PS" or if $R \leq 1.0$;

(c) It is considered as an "uncertain object" ($c = 3$) if $1.0 < R \leq 1.05$ and flag "E", or $1.05 < R < 1.10$ and flag "PS". These non-decidable cases can be resolved only with further data and/or analysis.

The overall classification picture for the whole GCC sample of Table 2 and the following ones is summarized in Fig. 7.
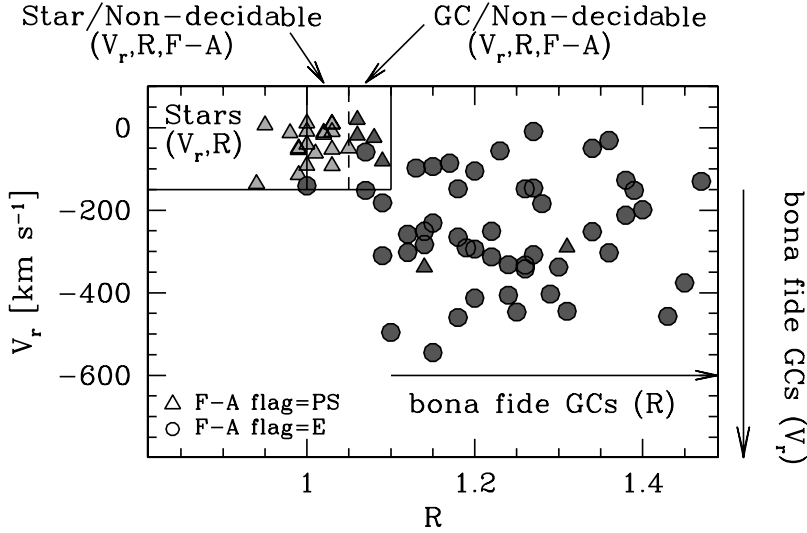
Fig. 7. Summary of the adopted classification criteria illustrated in the R vs. V_r diagram, where different symbols are used according to the value of the F-A flag of the targets. Circles represent extended objects (F-A flag = E) while triangles are point-like sources (F-A flag = PS). Bona fide stars ($c = 6$) are colored light-grey, bona fide GCs ($c = 1$) are plotted in darker grey, while the sources that cannot be firmly classified within our scheme ($c = 3$) are colored in the darkest grey. The box in the upper-left corner encloses stars and candidates whose nature requires the use of all the three parameters to be classified (V_r, R, F-A flag). The regions of the plot corresponding to different classifications are labeled. Note that most of the clusters with $R \geq 1.5$ (Tables 2 and 3) do not appear in this plot for clarity.

4.1.2. Image analysis for previously "confirmed" clusters with $V_r > -150.0$ km s^{-1}

The last 14 entries of Table 2 concern clusters previously confirmed by other authors, that have $V_r > -150.0$ km s^{-1}, i.e. a range of velocity that may suffer from contamination by MW stars. As noted in Sect. 4, those that have been confirmed only by virtue of their radial velocity may deserve further analysis to obtain a firm classification. According to the above criteria, 12 of these candidates are classified as genuine M 31 GC, one (B366) is classified as "uncertain" and one (B355) is classified as "bona fide star". Cluster B355 was classified as a confirmed GC by Perrett et al. (2002) relying only on its radial velocity. Object B216 will be discussed in detail in Sect. 4.3.

4.1.3. Image analysis for candidates with $V_r > -150.0$ km s^{-1}

The results of the image analysis for the 27 GCCs from our sample of Table 1 with $V_r > -150$ km s^{-1} are reported in Table 3. According to the above criteria, 7 of them are classified as genuine GCs (namely B162, B187, B189, B371, B388, B090D, and B255D), 17 are flagged as stars and 3 remain uncertain. We note that all the newly confirmed clusters are very clearly recognized as extended: all of them have flag = E and R ranges between 1.15 and 2.5. Note also that 5 of the 6 candidates in the range $-150 < V_r < -100$ km s^{-1} are genuine GCs, while for the 21 targets with $V_r > -100$ km s^{-1} we only detect 2 clusters and 16 bona fide stars. This further confirms how severely star contamination can affect observations in the range of V_r around $\sim -30 \pm 130$ km s^{-1}.

4.1.4. A few controversial objects

The three entries of Table 4 concern candidates that obtained different classifications from different authors. B055 was classified GC by P02, based on its radial velocity, while B00 classified it as a star. Our image analysis indicates unambiguously that B055 is an extended object, thus confirming the classification by P02. B121 was classified GC by H91 and "star" by B00 and our analysis does not help to resolve the controversy.

Object B409 was classified as a GC by F93, based on its radial velocity alone, and it was classified as a background galaxy

by Racine (1991), based on ground-based, high resolution imaging. Our morphological analysis of this object, and its low radial velocity, independently confirmed from Table 1 data, agree on clean point-source appearance; according to the adopted criteria, we classify it as a foreground star.

4.2. Background galaxy contamination

Since most of the known GCCs have been selected historically because of their fuzzy and/or extended appearance on photographic plates, it is natural that the major contamination source is represented by background galaxies, in particular those of spheroidal morphology. Any eye-detection survey is in fact reasonably safe with respect to low-redshift grand-design spirals, that can usually be confidently detected in good-quality images.

Spectrophotometric information can help to segregate with some confidence nucleated galaxies and M 31 GCs in the color domain. In G04 we noted, for instance, that the large majority of spurious GCCs, eventually identified as background galaxies, are redder than $(V - K) > 3.0$, so that by restraining target selection to bluer objects one should in principle maximize the detection of genuine clusters. This guess is supported on a more physical basis by looking at the expected photometric evolution of early- and late-type galaxy models by Buzzoni (2005), as shown in Fig. 8. On the other hand, the contribution of blue galaxy contaminants (closer in color to the bulk of low-metallicity M 31 GCs) may increase as far as our GC search extends to fainter and more blurred targets including poorer candidates in the Battistini et al. image-quality classification.

According to the updated RBC sample, the relative source partition of bona fide [galaxies: GCs: stars] among the entries with available V and K photometry and $(V-K) \geq 3.0$ is found to be [47:102:10], while the corresponding frequency blueward of the $(V - K)$ threshold is [11:202:27] . Taken at their face value, these numbers suggest that about 2/3 of the whole $(V - K) \geq 3.0$ GCCs might eventually be genuine clusters, while our performance should rise to nearly 85% for $(V - K) < 3.0$ candidates (see G04).

On the other hand, these figures are at odds with the empirical evidence from the present analysis, as for the whole sample of 71 GCCs of Table 1 with firm classification we find [galaxies: GCs: stars] = [12:42:17], with a remaining fraction of 5 Hɪɪ
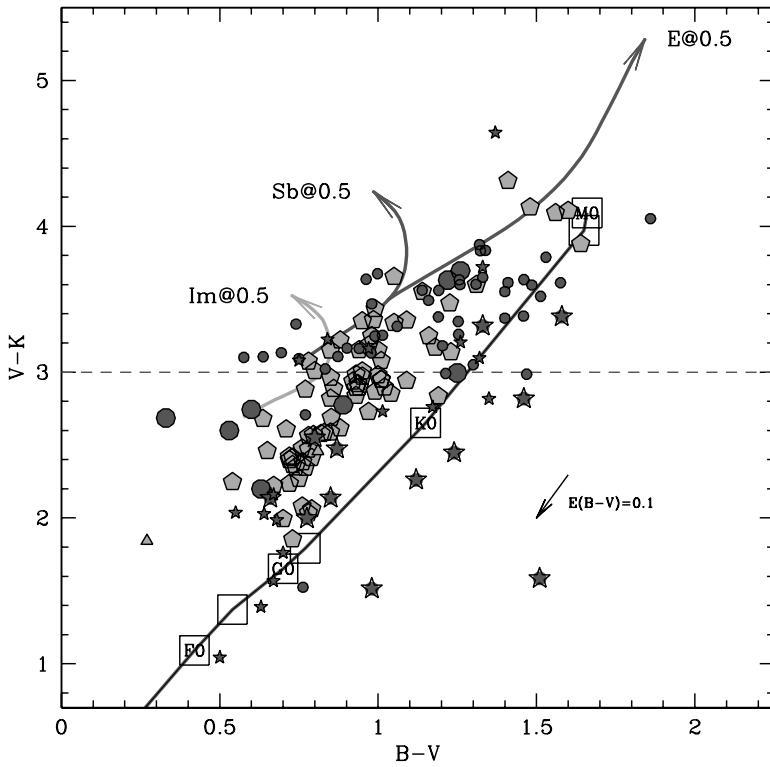
Fig. 8. Apparent $V - K$ vs. $B - V$ color distribution for the 45 targets of Table 1 with available B, V, K photometry (large symbols) compared to the corresponding RBC classification groups (small symbols). Large pentagons are the bona-fide ($c = 1$ RBC flag) M 31 globular clusters of this study, solid dots are background galaxies ($c = 4$), solid triangles mark M 31 HII regions ($c = 5$), and star markers are MW stellar interlopers ($c = 6$) and M 31 asterisms ($c = 7$). The arrow indicates the reddening vector corresponding to $E(B - V) = 0.1$. The main stellar locus for stars of different spectral type (F0, F5, G0, G5 dwarfs and K0, K5, and M0 giants from Johnson (1966) is superposed on the data, as well as the expected apparent colors vs. redshift for the Buzzoni (2005) template galaxy models for elliptical, spiral (type Sb) and irregular (type Im) Hubble types. Galaxy colors are tracked from $z = 0$ to 0.5 (as labeled on the plot). The stellar locus and the galaxy models *have been reddened* assuming $E(B - V) = 0.11$. Note that the main background contaminants of M 31 GCCs (i.e. ellipticals and nucleated spirals within $z \lesssim 0.2$) are always redder than $V - K = 3.0$ while only star-forming spirals and irregulars (as well as MW stars) become the prevailing contaminants at bluer colors.

regions and unclassified objects (again, see Fig. 8 for a summary). Thus, about one in two of our targets is a genuine globular, in spite of the fact that over 70% of our GCC sample is bluer than $(V - K) \geq 3.0$, and an a priori distribution should be expected such as [galaxies: GCs: stars] = [9:57:7] and 3 unclassified objects.

These figures lead us to the following conclusions:

(a) for deeper M 31 GCC surveys (that naturally include poorer and more "blurred" targets), the galaxy contamination becomes marginally more important, with an increasing contribution of blue spirals and star-forming systems. This is especially evident when we plot the galaxy $(V - K)$ distribution along the different Battistini et al. image-quality classification, as in Fig. 9. Fortunately, this bias can in principle be fully overcome as any spectroscopic identification would easily discriminate these spurious emission-line objects (note, for instance, that 9 out of 12 recognized galaxies in our Table 1 sample display some Balmer and/or [OIII] emission);

(b) between galaxy and star contaminants, the latter become increasingly important as class C-D-E Battistini et al. candidates are surveyed (we find 17 stellar interlopers vs. 7 expected cases).

4.3. Contamination by asterisms/associations

Radial velocities and image analysis are very effective tools to determine the most abundant sources of contamination, i.e. background galaxies, foreground stars and HII regions. However, they can be biased by a further and much subtler kind of contaminant. Small stellar associations, very young M 31 open clusters (whose integrated luminosity is dominated by a
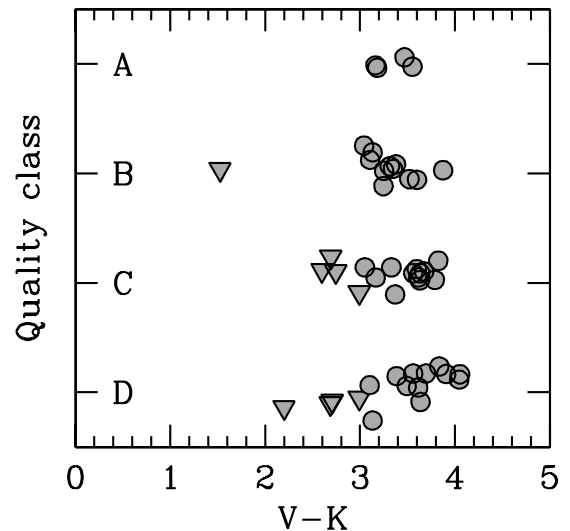
Fig. 9. The $V - K$ color distribution for confirmed background galaxies ($c = 4$ flag) in the whole RBC sample vs. original quality class according to the Battistini et al. (1980, 1982, 1987, 1993) scheme. Blue ($V - K < 3.0$) late-type galaxies (solid triangles) become an increasing contaminant source among class C–D cluster candidates.

few massive stars), and even perspective asterisms due to chance alignment of M 31 stars (and/or one or a few stars embedded in, or projected onto, a nebula) can easily mimic a typical faint GCC, when observed on low spatial-resolution images. Clearly, this class of contaminants is expected to affect faint and blue GCCs, especially those projected onto the disc of M 31. Cohen, Matthew & Cameron (2006) recently provided direct evidence
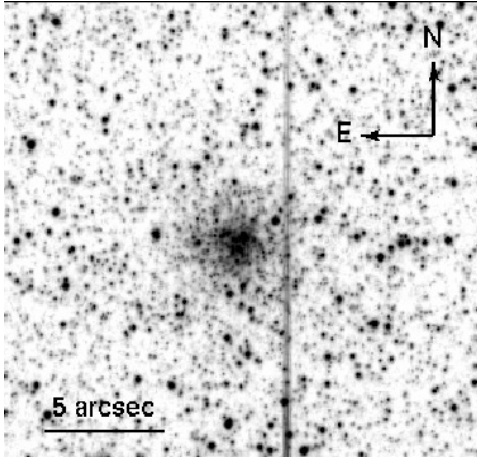
Fig. 10. The newly identified cluster B515 from *F606W* HST/ACS imagery. The scale and the orientation of the image are as reported.

of at least four such special cases among spectroscopically confirmed clusters, using high spatial-resolution images obtained with adaptive optics. To account for this "new" kind of contaminant, we introduce a new classification type, class $c = 7$, corresponding to asterisms/associations of M 31 stars.

In spite of the possible occurrence of these "fake" stellar aggregates, whose real occurrence needs to be more firmly assessed on a statistical basis, it is clear that, *in any case*, the final word on the real nature of M 31 GCCs must come from the physical resolution of the composing stars, through very high-resolution imaging (i.e., with the HST or with adaptive optics ground telescopes).

Among the clusters revealed to be asterisms by Cohen et al. (2006), there is one, B216, that we classify as a genuine GC in Table 2, based on its velocity and apparent morphology. While the other asterisms in the Cohen et al. list cannot be independently assessed from our low-resolution imagery, both the BFOSC and the DSS frames for B216 appear hardly compatible with the nearly empty field imaged by Cohen et al. However, we carefully checked the location of this field (with the collaboration of J. Cohen) and the listed target coordinates, and we conclude that B216 is indeed not a real cluster.

4.4. Independently checked candidates

As a duty cycle operation to maintain an updated release for the RBC, we periodically search the HST archive for intentional or serendipitous images of M 31 GCCs that can potentially reveal the true nature of the objects. A systematic survey of the available material is ongoing. Here we report only a few cases in which a clear and indisputable confirmation can be achieved from a thorough inspection of the images, i.e. objects partially resolved into stars or obvious foreground stars or asterisms.

– A new, clearly resolved, cluster has been identified by L.F. in deep *F555W* and *F814W* ACS/WFC images (see Fig. 10). The cluster has no counterpart in the RBC and is located at $\alpha_{2000} = 00^h42^m28.05^s$, $\delta_{2000} = 41°33'24.5''$. According to the nomenclature adopted in G04 and G05 we name the newly found cluster Bologna 515 (B515).
– The candidate B056D is clearly recognized as a genuine cluster on several deep (t_{exp} up to 2370 s) ACS/WFC images taken in different filters, by different teams.

– NB83, classified as genuine cluster by B00 based on its radial velocity ($V_r = -150 \pm 14.0$ km s^{-1}) is clearly recognized as a star in deep *F555W* and *F814W* images taken with the WFPC2. Note that the radial velocity is in the range where contamination by MW stars can occur (see Sect. 4.1).
– B102, classified as genuine cluster by H91 and P02 based on its radial velocity ($V_r = -235.4 \pm 11.7$ km s^{-1}) is recognized as an asterism formed by two stars superposed on a nebulosity in deep ACS/WFC images taken in different filters.
– The candidate NB92 is recognized as a bright (likely foreground) star in deep ACS/WFC and in shallow WFPC2 images taken in various filters.
– The candidate B162, that we classified as a genuine cluster based on its radial velocity ($V_r = -146 \pm 8$ km s^{-1}) and on its extendedness (see Table 3), is clearly recognized as a genuine cluster also on several deep (t_{exp} up to 2370 s) ACS/WFC images taken in different filters, by different teams.
– The candidate G137, that we recognized as an HII region from its spectrum, appears as a bright point-source surrounded by an asymmetric nebula on deep ACS/WFC images, thus confirming our spectroscopic classification.
– B118[7], NB99, NB100, NB106, classified as stars in the RBC are recognized as stars also in deep ACS/WFC images, thus confirming the existing classification on a much firmer basis.

In summary, we identified a new cluster (B515), one candidate is recognized as a genuine cluster (B056D), two objects previously believed to be genuine clusters were re-classified as foreground star and asterism (NB83 and B102, respectively), one candidate has been firmly classified as a star (NB92), and the existing classification of seven other objects (B118, B162, B137, NB99, NB100 and NB106) has been fully confirmed.

5. An updated sample of confirmed M 31 GCs

As a result of our spectroscopic and imaging survey of Table 1 candidates, we have provided 42 newly confirmed bona fide M 31 clusters, while a total of 34 GCCs should be among background galaxies, foreground stars or HII regions. Our study increases the total number of confirmed M 31 GCCs from 337 to 368 and the number of confirmed GCs having a radial velocity estimate from 313 to 349.

While a thorough analysis of the integrated properties (including Lick indices) of the newly confirmed clusters will be given in Paper II of this series (see Sect. 1), a first glance at their stellar populations is provided in Fig. 11, where we compare the new GCs with the already confirmed ones (from G04) and with the Buzzoni (1989) theoretical models for Simple Stellar Populations (SSPs), in the reddening-corrected $J - K$ vs. $B - K$ plane (see James et al. 2006, for a thorough discussion of this diagnostic plane). Most of the new clusters have the typical integrated colors of classical old globulars, and they appear to span the whole metallicity range covered by previously known M 31 GCs.

In terms of GC luminosity function, our survey provides a strong contribution in the $17.0 < V \le 18.0$ range, where we add 30 new clusters to the 120 previously known objects (see Fig. 12). The 42 newly confirmed clusters are distributed along all of the Battistini at al. classes from A to D[8], but we increased (+75%) the surveyed fraction of class D candidates.

---

[7] See updates and revisions http://www.bo.astro.it/M31/.
[8] Specifically, the quality-class distribution results [A:B:C:D:E] = [13:10:4:15:0].
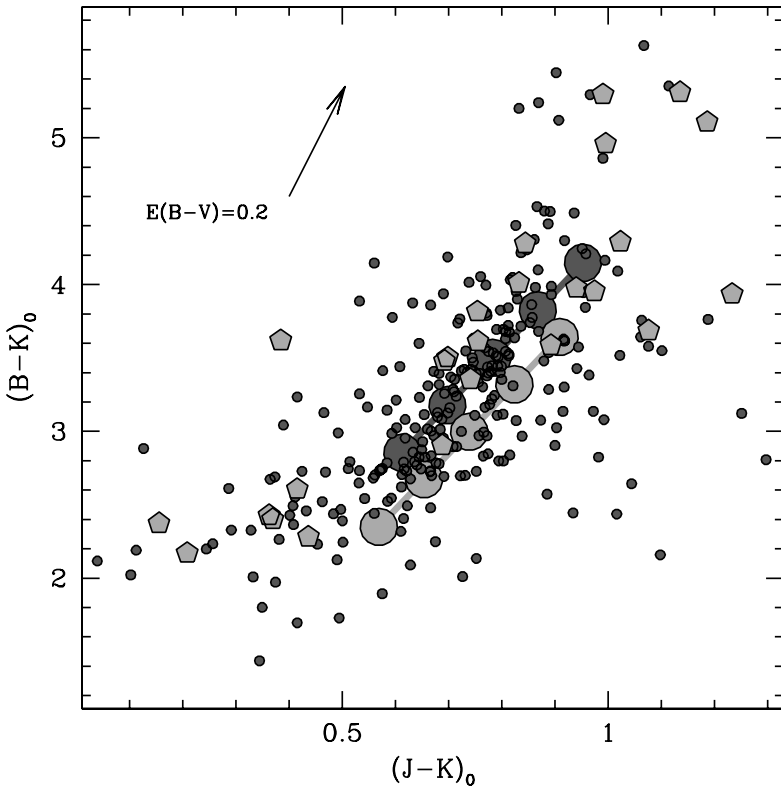
Fig. 11. Distribution of confirmed M 31 clusters in the reddening-corrected $J - K$ vs. $B - K$ plane. $E(B - V) = 0.11$ is assumed for all M 31 clusters. Small filled circles are previously confirmed clusters, pentagons are the newly confirmed clusters studied in the present paper. SSP model sequences by Buzzoni (1989), for fixed ages (i.e. 15 Gyr for the upper sequence and 2 Gyr for the lower sequence) and varying metallicity (from [Fe/H] = −2 to a solar value, at equal steps of 0.5 dex, see large solid dots in the sense of increasing $J - K$ color along the sequences) are superposed. A Salpeter IMF slope and a red horizontal branch morphology is assumed in the models.
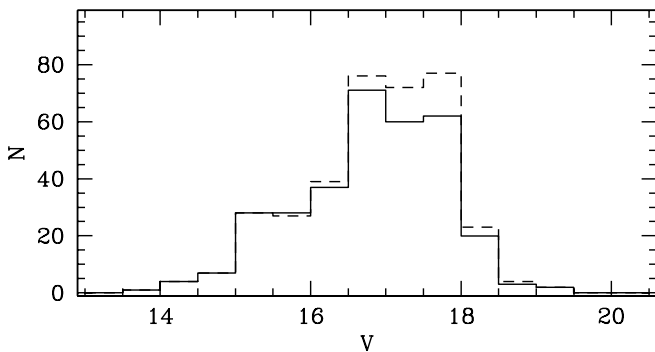
Fig. 12. The V luminosity function of confirmed M 31 clusters. Continuous and dashed lines show the distributions *before* and *after* the present survey, respectively. Most of the new additions (15 out of 42) are for class D candidates according to the Battistini et al. classification scheme.

Only 172 candidates of class D and E have been scrutinized to date. Since 67 of them turn out to be genuine clusters (∼35%) and ∼500 candidates of these classes still need to be confirmed, likely over 100 genuine clusters are still hidden in this harvest of "intermediate/low-quality" targets. Hence, large surveys, such as the one presented in this paper, are needed to reach a complete sample of M 31 clusters.

5.1. A basic application: the M 31 mass estimate

A preliminary application of the basic kinematical properties of our enlarged sample provides results in excellent agreement with the more specific analysis by P02. The mean systemic velocity of the M 31 GC system (after a 2-σ clipping procedure) is

$\langle V_{GC} \rangle = -296 \pm 12$ km s^{-1}, the median is -297 ± 14 km s^{-1}. The overall velocity dispersion is $\sigma = 158 \pm 10$ km s^{-1}.

In Fig. 13 we show the distribution of the M 31-centric velocities of confirmed GCs as a function of the projected distance from the center along the major axis of the galaxy (X, see G04, and references therein). To obtain a more easily readable plot we limited the sample to the range -30 kpc $< X < +30$ kpc, while the outermost cluster in our catalog (B514, see G00) lies at $X = 59.6$ kpc[9].

The well known rotation pattern of M 31 GCs (see van den Bergh 2000, P02, and references therein) is clearly visible in Fig. 13, with a flattening occurring for $|X| \gtrsim 7$ kpc. Averaging and 2-σ clipping velocities as a function of X in boxes 4 kpc wide, we obtain an amplitude of the overall rotation pattern of 134 ± 15 km s^{-1}, again in very good agreement with P02.

As an example of the possible applications of the newly obtained large and homogeneous database of radial velocities of M 31 GCs, we obtained a simple estimate of the mass of M 31 within $R \simeq 60$ Kpc, using the Projected Mass Estimator (PME, Bahcall & Tremaine 1981). Adopting the version by Heisler et al. (1985) of the PME

$$M_P = \frac{C}{\pi G N} \sum_i^N V_i^2 r_i \qquad (1)$$

and assuming an isotropic velocity distribution ($C = 32$), P02 obtained for M 31 a total mass $M_{tot} = 4.1 \pm 0.1 \times 10^{11}$ $M_\odot$, by using 319 dynamical probes (GCs) out to a radius of $\simeq 27$ kpc from the galaxy center. Under the same assumptions, from our enlarged sample of 349 GCs out to ∼60 kpc from the galaxy center (projected distance, R_p), we obtain $M_{tot} = 4.4 \pm 0.2 \times 10^{11}$ $M_\odot$.

---

[9] For M 31 we adopt a distance modulus $(m - M)_0 = 27.47$, from McConnachie et al. (2005), and $E(B - V) = 0.11$, as in G04. This corresponds to a distance $D = 783$ kpc.
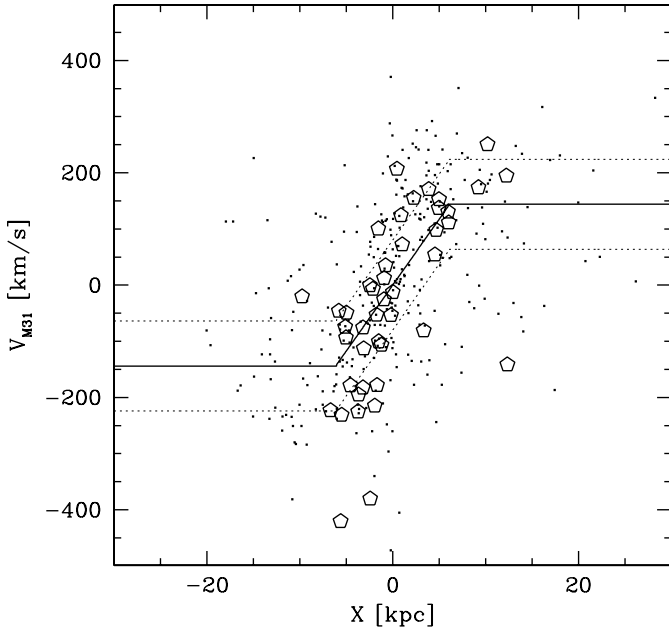
Fig. 13. Radial velocity of the M 31 globular clusters (corrected for the systemic velocity of M 31) vs. the projected distance along the major axis (X). Pentagon markers represent the newly confirmed clusters studied in the present paper. The continuous line is a fit to the 2-σ clipped mean velocity as a function of major-axis projected distance, computed on 4 kpc wide boxes shifted by 1 kpc steps in X. 2-σ contours are plotted as dotted lines.

The uncertainties on the actual isotropy degree of the underlying velocity distribution contribute an additional factor ∼2 to the quoted uncertainties. The estimate is unchanged if we exclude from the sample the presumably young clusters identified in Fusi Pecci et al. (2005) as belonging to the thin disc of M 31. The obtained value is well within the range spanned by the most recent estimates of the mass of M 31, as listed by Evans & Wilkinson (2000) in their Table 6. The agreement with previous estimates obtained using GCs as tracers (Federici et al. 1993, P02) is also quite good.

The Bahcall & Tremaine (1981) PME was originally conceived for test particles to probe a central point-mass gravitational source. As an exercise, we can approach this condition by restraining our analysis to the 14 most distant clusters in our sample, with $R_p > 20.0$ kpc, and maintain the isotropy hypothesis (i.e. $C = 16$, in Eq. (1) above). With these constraints we obtain $M_{tot} = 4.3–7.0 \times 10^{11}$ $M_\odot$, where the reported range has been obtained by a *jackknife* resampling technique (Lupton 1993). This estimate is in good agreement with the results by Federici et al. (1993) and with the recent independent estimates by Carignan et al. (2006) and Chapman et al. (2006).

The above estimates rely on methods that assume that the adopted tracers follow the mass density profile of the probed potential, that is not the case for GCs systems, in general. To overcome this problem Evans et al. (2003) introduced a new mass estimator that does not require coupling between the distribution of the tracers and the underlying mass distribution. As an example of its application, Evans et al. (hereafter E03) provide an estimate of the mass of M 31 based on GCs, obtaining $M = 1.2 \times 10^{12}$ $M_\odot$. With the same assumptions as Evans et al. we obtain $M_{rot} = 2.9 \times 10^{11}$ $M_\odot$ for the rotational component (to compare with $M_{rot} = 3.0 \times 10^{11}$ $M_\odot$ found by E03) and $M_{pres} = 2.1 \times 10^{12}$ $M_\odot$ for the pressure component (to compare with $M_{pres} = 0.9 \times 10^{12}$ $M_\odot$ found by E03). The total mass is

$M = 2.4 \times 10^{12}$ $M_\odot$, a factor of 2 larger than the E03 estimate. Part of this difference is due to the larger value of the M 31 distance adopted here than E03. Our experiments, however, indicate that the results from this method are sensitive to the way in which the rotational and pressure components are separated: the very simple rotation pattern adopted here (see Fig. 13) introduces a large uncertainty in our result. Once the above factors are taken into account the agreement with E03 is satisfying, at least in this preliminary stage of the analysis.

A detailed analysis of the kinematics of the M 31 GC system and the galaxy mass profile is deferred to the completion of our remote-cluster search, currently in progress (see Galleti et al. 2005).

6. Summary and conclusions

We have presented the first results of a large spectroscopic and imaging survey of candidate clusters in M 31. The survey allowed us to confidently classify 76 candidates whose nature was previously unknown: 42 of these are new M 31 GCs, while 12 have been recognized as background galaxies, 2 are M 31 HII regions, and the remaining 17 objects are foreground stars and 3 unclassified objects (possibly M 31 clusters or foreground stars). An estimate of the radial velocity has been obtained for all the 42 newly recognized clusters as well as for an additional sample of 55 M 31 GCs previously confirmed by other authors and two controversial objects. The various sets of radial velocities for M 31 GCs available in the literature has been reported to the same scale, multiple measures have been averaged (see Sect. 3.2 for details), and a final merged catalog has been produced (see Table 5, online material). The present analysis has increased the sample of confirmed M 31 clusters from 337 to 369 members, and the number of confirmed GCs with a radial velocity estimate is increased from 313 to 349.

While the main basis for the classification work was provided by radial velocities, we have also implemented a method to distinguish between point and extended sources on low-resolution imaging that allows us – in many cases – to disentangle genuine M 31 clusters and MW stars when radial velocity alone leads to controversial conclusions. We also provide a reliable classification for few candidates not included in our survey based on the inspection of publicly released high spatial resolution images from the HST general archive.

6.1. The revised Bologna catalog V2.0

All the present observational material has been consistently used to update the RBC, now available on line in its latest V2.0 release. Future minor updates of the catalog will be described and commented on the RBC web page (http://www.bo.astro.it/M31/) where the catalog database can be retrieved as ASCII files.

References

Baade, W., & Arp, H. 1964, ApJ, 139, 1027
Bahcall J. N., & Tremaine S. 1981, ApJ, 244, 805

Barmby, P., & Huchra, J. P. 2001, AJ, 122, 2458
Barmby, P., Huchra, J. P., Brodie J. P., et al. 2000, AJ, 119, 727
Barmby, P., Huchra, J. P., & Brodie, J. P. 2001, AJ, 121, 1482
Battistini, P. L., Bonoli, F., Braccesi, A., et al. 1980, A&AS, 42, 357
Battistini, P. L., Bonoli, F., Buonanno, R., Corsi, C. E., & Fusi Pecci, F. 1982, A&A, 113, 39
Battistini, P. L., Bonoli, F., Braccesi, A., et al. 1987, A&AS, 67, 447
Battistini, P. L., Bonoli, F., Casavecchia, et al. 1993, A&Ap, 272, 77
Beasley, M. A., Brodie, J. P., Strader, J., et al. 2004, AJ, 128, 1623
Bellazzini, M., Cacciari, C., Federici, L., Fusi Pecci, F., & Rich, M. 2003, A&A, 405, 867
Bertin, E., & Arnouts, S. 1996, A&AS, 117, 393
Brown, T. M., Ferguson, H. C., et al. 2004, ApJ, 613, 125
Buonanno, R., Corsi, C. E., Battistini, et al. 1982, A&AS, 47, 451
Buzzoni, A. 1989, ApJS, 71, 817
Buzzoni, A., 2005, MNRAS, 361, 725
Carignan, C., Chemin, L., Hutchmeler, W. K., & Lockman, F. J., 2006, ApJ, 641, L109
Chapman, S. C., Ibata R., Lewis G. F., et al. 2006, ApJ, in press
    [arXiv:astro-ph/0602604]
Cohen J. G., Matthews K., & Cameron P. B. 2006, ApJ, 634, L45
Crampton, D., Cowley, A. P., Schade, D., & Chayer, P. 1985, ApJ, 288, 494
Diaz, A. I., Terlevich, E., Pagel, B. E. J., Vilchez, J. M., & Edmunds, M. G. 1987, MNRAS, 226, 19
Djorgovski, S.G. 1993, in Structure and Dynamics of Globular Clusters, ed. S. G. Djorgovski & G. Meylan (S. Francisco: ASP) ASP Conf. Ser., 50, 373
Dubath, P. & Grillmair, C. J. 1997, A&A, 321, 379
Durrell, P. R., Harris, W. E., & Pritchet, C.J., 2004, AJ, 128, 260
Evans, N. W., & Wilkinson, M. I. 2000, MNRAS, 316, 929
Evans, N. W., Wilkinson, M. I., Perrett, K. M., & Bridges, T. J. 2003, ApJ, 583, 752
Federici, L., Bonoli, F., Ciotti, L., et al. 1993, A&A, 274, 87
Fusi Pecci, F., Buonanno, R., Cacciari, et al. 1996, AJ, 112, 1461
Fusi Pecci, F., Bellazzini, M., Buzzoni, A., et al. 2005, AJ, 130, 554
Galleti, S., Federici, L., Bellazzini, M., et al. 2004a, A&A, 416, 917 (G04)
Galleti, S., Bellazzini, M., Federici, L., & Fusi Pecci, F. 2005, A&A, 436, 535
Gualandi, R., & Merighi, R. 2001, Manual Reports,
    http://www.bo.astro.it/~loiano/TechPage/pagine/
    BfoscManualTechPage/BfoscManual.htm
Heisler J., Tremaine S., & Bahcall J. N., 1985, ApJ, 298, 8
Holland, S., Fahlman, G. G., & Richer, H. B. 1996, AJ, 112, 1035
Hubble, E. P. 1932, ApJ, 76, 44
Huchra, J., Stauffer, J., & van Speybroeck, L. 1982, ApJ, 259, L57
Huchra, J. P., Brodie, J. P., & Kent, S. M. 1991, ApJ, 370, 495

Huxor, A., Tanvir, N. R., & Irwin, M. J. 2004, in Satellites and Tidal tails, ed. F. Prada, D. Martinez-Delgado & T. Mahoney (S. Francisco: ASP), ASP Conf. Ser., 327, 118
Huxor, A. P., Tanvir, N. R., Irwin, M. J. et al. 2005, MNRAS, 360, 1007
Jablonka, P., Bica, E., Bonatto, C., et al. 1998, A&A, 335, 867
James, P. A., Salaris, M., Davies, J.I., Phillipps, S., & Cassisi, S. 2006, MNRAS, 367, 339
Johnson, H. L., 1966, ARA&A, 4, 193
King, I. R. 1966, AJ, 71, 276
Koo, D. C., Kron, R. G., Nanni, D., Trevese, D., Vignato, A. 1986, AJ, 91, 478
Kron R. G., 1980, ApJS, 43, 305
Laird J. B., Rupen M. P., Carney B. W., & Latham D. W. 1988, AJ, 96, 1908
Lupton R., 1993, Statistics in theory and practice (Princeton: Princeton University Press)
McConnachie, A. W., Irwin, M. J., Ferguson, A. M. N., et al. 2005, MNRAS, 356, 979
Mochejska, B. J., Kaluzny, J., Krockenberger, M., Sasselov, D. D., & Stanek, K. Z. 1998, Acta Astron., 48, 455
Molinari, E., Buzzoni, A., & Chincarini, G. 1990, MNRAS, 246, 576
Perrett, K. M., Bridges, T. J, Hanes, D. A., et al. 2002, AJ, 123, 2490
Peterson, R. C., 1989, in Dynamics of dense stellar systems, ed. D. Merritt (Cambridge: Cambridge Univ. Press), 161
Puzia, T. H., Perrett, K. M., & Bridges, T. J. 2005, A&A, 434, 909
Racine, R. 1991, AJ, 101, 865
Rich, R. M., Reitzel, D. B., Guhathakurta, P., Gebhardt, K., & Ho, L. C. 2004, AJ, 127, 2139
Rich R.M., Corsi C. E., Cacciari C., Federici L., Fusi Pecci F., Djorgovski S. G., & Freedman, W. L. 2005, AJ, 129, 2670
Robin, A. C., Reylè, C., Derriére, S., & Picaud, S. 2003, A&A, 409, 523
Sargent, W. L. W., Kowal, C. T., Hartwick, F. D. A., & van der Bergh, S. 1977, AJ, 82, 947
Sharov, A. F., Lyutyi, V. M., & Esipov, V. F. 1995, PAstL, 21, 240
Skrutskie M. F., Cutri, R. M., Stirning, R., et al. 2006, AJ, 131, 1163
Telting, J. & Corradi, R. 2000, Isaac Newton Group of Telescopes, Autofib2/WYFFOS User Manual
Tonry, J., & Davis, M. 1979, AJ, 84, 1511
Trager, S.C., Worthey, G., Faber, S.M., Burstein, D., & González, J.J 1998, ApJS, 116, 1
van den Bergh, S. 1967, AJ, 72, 70
van den Bergh, S. 1969, ApJS, 19, 145
van den Bergh, S. 2000, The galaxies of the Local Group (Cambridge: Cambridge University Press)
Vetešnik, M. 1962, Bull. Astron. Inst. Czecho., 13, 180